Microscopy, 2022, **71(S1)**, i132–i147
DOI: https://doi.org/10.1093/jmicro/dfab026
Special Issue Paper

MICROSCOPY

Evolution in X-ray analysis from micro to atomic scales in aberration-corrected scanning transmission electron microscopes

M. Watanabe[1,*] and R.F. Egerton[2]

[1]Department of Materials Science and Engineering, Lehigh University, 5 East Packer Avenue, Bethlehem, PA 18015-3195, USA
[2]Department of Physics, University of Alberta, Edmonton, AB T6G 2E1, Canada
[*]To whom correspondence should be addressed. E-mail: masashi.watanabe@lehigh.edu

Abstract

X-ray analysis is one of the most robust approaches to extract quantitative information from various materials and is widely used in various fields ever since Raimond Castaing established procedures to analyze electron-induced X-ray signals for materials characterization '70 years ago'. The recent development of aberration-correction technology in a (scanning) transmission electron microscopes (S/TEMs) offers refined electron probes below the Å level, making atomic-resolution X-ray analysis possible. In addition, the latest silicon drift detectors allow complex detector arrangements and new configurational designs to maximize the collection efficiency of X-ray signals, which make it feasible to acquire X-ray signals from single atoms. In this review paper, recent progress and advantages related to S/TEM-based X-ray analysis will be discussed: (i) progress in quantification for materials characterization including the recent applications to light element analysis, (ii) progress in analytical spatial resolution for atomic-resolution analysis and (iii) progress in analytical sensitivity toward single-atom detection and analysis in materials. Both atomic-resolution analysis and single-atom analysis are evaluated theoretically through multislice-based calculation for electron propagation in oriented crystalline specimen in combination with X-ray spectrum simulation.

Key words: quantitative analysis, ζ-factor method, aberration-corrected STEM, silicon drift detector, atomic-resolution analysis, single-atom characterization

Introduction

Characteristic X-rays are emitted from a specimen as a result of inelastic interactions with incident electrons. Ever since Raimond Castaing established procedures to use the generated characteristic X-ray signals for characterizing materials ∼'70 years' ago [1], X-ray analysis has been one of the essential characterization tools to extract quantitative information from various materials and is widely used in various fields, i.e. for bulk-material samples in scanning electron microscopes (SEMs) or electron-probe microanalyzers (EPMAs) [e.g. 2] and for electron transparent thin film specimens in (scanning) transmission electron microscopes (S/TEMs) or analytical electron microscopes (AEMs) [e.g. 3].

The recent development of aberration-correction technology in S/TEM has brought a paradigm shift in materials characterization. Both in STEM and TEM imaging, sub-Å resolution is routinely available. Ultimately, the latest aberration-corrected microscopes offer half-Å resolution both in the STEM and TEM modes [4,5]. Especially in STEM, aberration correction provides a refined incident probe size without reducing the probe current significantly, which is essential for superior chemical analysis through X-rays and energy-loss electrons. In fact, it is now possible to carry out electron energy-loss spectrometry (EELS) mapping at atomic resolution on a routine basis [e.g. 6–13]. The use of an aberration-corrected fine probe is also ideal for X-ray energy-dispersive spectrometry (XEDS), since the aberration correction makes it possible to reduce the incident probe size while maintaining higher currents. The aberration-corrected probe offers improvement not only in spatial resolution but also in analytical sensitivity. In a previous study [14], it was demonstrated that the spatial resolution of X-ray analysis is improved to ∼0.4 nm and the detectability limit approaches a few atoms, implying that atomic-level analysis/mapping by X-ray analysis is feasible in aberration-corrected STEM.

Conventionally, X-ray signals in an S/TEM instrument are significantly limited by weak signal generation, which could be worse in an aberration-corrected instrument than a conventional one because the analytical volume sizes are generally much smaller due to the reduced probe size. X-ray signal generation is also fundamentally limited by the ionization and de-excitation processes, which are described by an ionization cross section and the fluorescence yield, respectively. In addition, traditional XEDS spectrometer geometries restrict X-ray signal collection in the S/TEM instruments, i.e. typical solid angles for signal collection in S/TEM with a conventional Si(Li) detector were ∼0.1–0.2 sr, which is equivalent to only 1–2% of the entire X-ray signal generated from a thin specimen and ∼100 times worse than that in EELS. Hence, higher probe currents were required for X-ray analysis to compensate the poor signal generation and the poor signal

Received 7 June 2021; Revised 30 June 2021; Editorial Decision 5 July 2021; Accepted 14 July 2021

correction. Since higher probe current enlarges the incident probe size, spatial resolution for X-ray analysis is generally degraded. But despite inefficient signal generation and collection aspects, X-ray analysis in S/TEM is a very robust and important approach for materials characterization, due to the simple nature of its operation and analysis. As mentioned above, X-ray generation can be enhanced to some degree by using a refined probe with additional current in an aberration-corrected STEM instrument.

Obviously, improvement of the signal correction efficiency is rather crucial for advances in X-ray analysis in a modern S/TEM instrument. Several attempts have been proposed and applied by redesigning X-ray detector configurations: i.e. modification of detector locations [e.g. 15,16], construction of multiple-array detector systems [17] and development of large solid-angle detectors [18]. The recently developed silicon drift detectors (SDDs) are relatively amenable to the fabrication of complex detector arrangements with new configurational designs, which have been incorporated into the latest aberration-corrected instruments. The collection solid angles exceed 1 sr or even π sr in the latest aberration-corrected S/TEM instrument [19,20]. Therefore, significant improvements in X-ray analysis (in terms of spatial resolution and analytical sensitivity) are expected by using the latest aberration-corrected STEM instruments with the improved X-ray detector configuration.

In this review paper, recent progress and advantages related to S/TEM-based X-ray analysis will be discussed: (i) progress in quantification for materials characterization including the recent applications to light element analysis, (ii) progress in analytical spatial resolution for atomic-resolution analysis and (iii) progress in analytical sensitivity toward single-atom detection and analysis in materials. Both atomic-resolution analysis and single-atom analysis are evaluated theoretically through multislice-based calculation for electron propagation in oriented crystalline specimen in combination with X-ray spectrum simulation.

Progress in quantification procedures for X-ray analysis

Conventional quantitative X-ray analysis in S/TEM

The characteristic X-ray intensity excited by incident electrons is closely related to the amount of the corresponding element. Raimond Castaing, 'the father of X-ray analysis', established the theory of quantitative X-ray analysis with his development of a so-called matrix correction, which includes X-ray absorption and fluorescence effects [1]. Castaing's approach is known as the ZAF correction and became the standard procedure for quantitative X-ray analysis of bulk samples in SEM and EPMA. A similar concept is applicable to the electron transparent thin specimens in S/TEM, i.e. local compositions can also be quantified by measuring the characteristic X-ray signals from the thin specimens, with a much simpler form than the ZAF matrix correction for bulk samples. Cliff and Lorimer proposed a ratio method for quantitative X-ray analysis of thin-foil specimens [21]:

$$\frac{C_A}{C_B} = k_{AB}\left(\frac{I_A}{I_B}\right) \tag{1}$$

where C_A and C_B are compositions of two constituent elements (typically defined as the weight fraction or wt.%), I_A and I_B are the characteristic X-ray intensities from these elements, and k_AB is the Cliff–Lorimer *k* factor: a sensitivity factor always defined with respect to the base element (in this case, element B). The Cliff–Lorimer *k* factors can be determined both theoretically and experimentally [e.g. 3,22]. Due to its simplicity, the Cliff–Lorimer ratio method has been applied widely. However, X-ray absorption can be one of the most serious problems for quantification, even in thin specimens. In fact, the X-ray absorption correction for thin specimens in S/TEM is harder than that for bulk samples in SEM/EPMA because prior information of a finite specimen thickness and density at individual analysis points is required. Although application of the Cliff–Lorimer ratio method is straightforward, it is rather challenging to achieve sufficient enough accuracy and precision in quantitative X-ray analysis of a thin specimen in some cases.

Improved quantitative X-ray analysis in S/TEM: the ζ (zeta) factor method

The X-ray absorption can be one of the major limitations in the accurate quantitative analysis of thin specimens. In order to correct the X-ray absorption, independent measurements of the specimen thickness and density are required, which are time consuming and could induce additional errors in quantification. In order to remove the burden of thickness determination and to improve accuracy and precision in quantification, a quantification procedure for thin specimens, so-called the ζ-factor method, was developed [23–25]. For a thin-film specimen, the measured characteristic X-ray intensity is proportional to the mass thickness ρt and elemental concentration, unless the generated X-ray signals are affected by absorption and fluorescence. Therefore, the following relationship can be established between the mass thickness and the measured X-ray intensity [23]:

$$\rho t = \zeta_A \frac{I_A}{C_A D_e} \tag{2}$$

where ζ_A is a proportionality factor that connects I_A with ρt and C_A, and D_e is the number of primary electrons: probe current times acquisition time (so beam-current measurement is essential for this approach). The ζ-factor is related to X-ray generation and detection, thus it is equivalent to the atomic number term, *Z* in the ZAF matrix correction for bulk sample analysis.

Similar relationships to the above equation hold for other elements in a thin specimen, and hence the composition for an Element *X* and the mass thickness can be expressed as:

$$C_X = \frac{\zeta_X I_X}{\sum \zeta_j I_j},\ \rho t = \frac{\sum \zeta_j I_j}{D_e} \tag{3}$$

The composition and mass thickness can be determined simultaneously by measuring all of the X-ray intensities from a thin specimen.

When some of the X-rays are absorbed and/or fluoresced significantly in the specimen, absorption and fluorescence correction terms are easily incorporated into Eq. (3). For example, an absorption-correction term A_X for an X-ray line X can be added as [23,26]:

$$C_X = \frac{\zeta_X A_x I_X}{\sum \zeta_j A_j I_j}, \rho t = \frac{\sum \zeta_j A_j I_j}{D_e} \tag{4}$$

$$A_X = \frac{(\mu/\rho)^X_{sp}\,\rho t \csc\alpha}{1 - exp\left[-(\mu/\rho)^X_{sp}\,\rho t \csc\alpha\right]}$$

where $(\mu/\rho)^X_{sp}$ is the mass absorption coefficient of the characteristic X-ray Line X in the specimen and A is the detector take-off angle.

The ζ-factor method has been available in several commercial XEDS systems [27,28] and in the free software package DTSA II [29]. It should be noted that there are similar quantification approaches, for example a partial cross section approach [30].

Selected applications of the ζ-factor method for materials characterization

Information about local specimen thickness determined through the ζ-factor method is essential for the absorption correction. Furthermore, the thickness information is beneficial to extract additional information for materials characterization, including the analyzed volume, the number of constituent atoms, etc. as described in the original ζ-factor paper [23].

As an example of quantitative analysis by the ζ-factor method, Fig. 1 shows a set of X-ray maps taken from a selected region in a Cr/Cu/Ni/Au multilayer thin film annealed at 573K for 300 s: (i) annular dark field (ADF)-STEM image; (ii) thickness, t map; (iii) spatial resolution, R map; (iv) Cu composition map; (v) Ni composition map and (vi) Au composition map [31]. Ni was placed between Cu and Au layers as a barrier layer to prevent any reaction between Cu and Au. However, after such a relatively short annealing at a low temperature, some amounts of Cu and Au (~15 at%) can be found in the Au and Cu layers, respectively, although no evident interdiffusion of Cu or Au was found at the Cu/Ni and Ni/Au interfaces. In other words, the barrier Ni layer remained as deposited but both Cu and Au were transported to the counter part through the Ni layer. The interdiffusion behaviors at the Cu/Ni and Ni/Au interfaces can also be evaluated by local spatial resolution R values. In general, there could be no significant atomic interdiffusion at an interphase interface if a composition variation with at the interface is close to an estimated R value. The spatial resolution map was calculated using the Gaussian beam-broadening model proposed by Van Cappellen and Schmitz [32], which requires the probe diameter and electron broadening in a thin specimen. Since this beam broadening is a function of the compositions and thickness, the ζ-factor method can also provide the broadening and hence spatial resolution at individual pixels in a map. As shown in the R map in Fig. 1c, the R value is ~ 2 nm both at the Cu/Ni and Ni/Au interfaces, which is very similar to the composition variation widths at those interfaces estimated from the composition maps. Therefore, there is no significant interdiffusion between Cu and Ni and between Ni and Au, respectively.

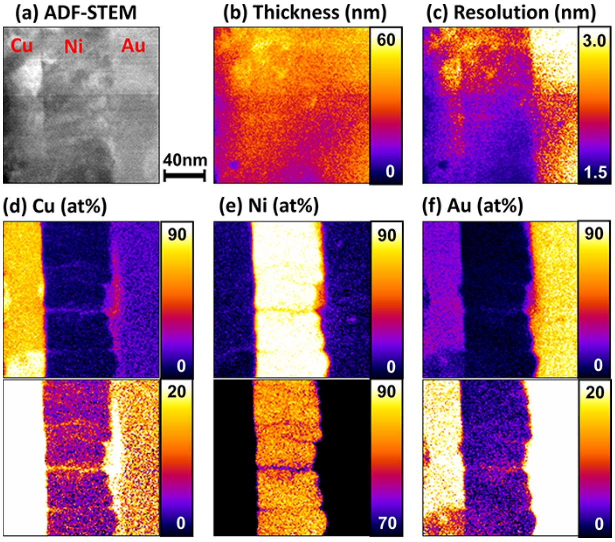

Fig. 1. Summary of X-ray maps from a Cr/Cu/Ni/Au annealed at 573K for 300 s, quantified by the ζ-factor method: (a) ADF-STEM image, (b) thickness, t map, (c) spatial resolution, R map, (d) Cu map, (e) Ni map and (f) Au map [31]. There are two versions of the composition maps with different composition ranges to show details of atomic segregation.

Other versions of the composition map, with limited composition ranges, show the details of the elemental distributions in Fig. 1d–f. The Ni composition is depleted and correspondingly the Cu and Au compositions are enriched at certain regions in the Ni layer, which correspond to the grain boundaries (GBs) according to the ADF-STEM image (Fig. 1a). Thus, both Cu and Au could be transported through the Ni layer by GB diffusion instead of bulk diffusion [31]. Quantitative X-ray mapping directly proves the boundary diffusion of Cu and Au in the multilayer thin-film system. In order to understand mechanisms of the GB diffusion, it is important to determine the amounts of Cu and Au in Ni GBs. However, the compositions of Cu and Au in the boundaries vary depending on the specimen thickness, the boundary inclination and the incident probe size used for analysis, meaning that segregant compositions are no longer quantitative values for the grain boundary characterization. A better way to characterize the boundary segregation is to employ the boundary enrichment Γ^{ex} (defined as a number of excess atoms per unit area in a boundary plane) instead of the simple composition since the boundary coverage is less sensitive to the analytical conditions mentioned above. Furthermore, determination of Γ^{ex} requires no prior knowledge of the boundary width – the measurement of which may produce further errors. From the compositions of solute Element A and major Element B, the boundary enrichment for A can be converted using the following equation [25]:

$$\Gamma^{\mathrm{ex}}_{\mathrm{A}} = \mathrm{N}_{\mathrm{B}} \frac{X^{gb}_{A} - X^{bk}_{A}}{X_{\mathrm{B}}} \frac{V}{A} \tag{5}$$

where N_{B} is the number of B atoms per unit volume in the surrounding bulk region, ${X_A}^{gb}$ and ${X_A}^{bk}$ are the atomic fractions of Element A at the GB and the bulk region, respectively, X_{B} is the atomic fraction of Element B, and V and A are the interaction volume and the area of the boundary inside the interaction volume, respectively. An accurate estimation of the V/A term is essential to remove the influence of specimen thickness on the Γ^{ex} determination. To calculate the V/A term, the specimen thickness t is required again, and can be provided by the ζ-factor method [23,25].

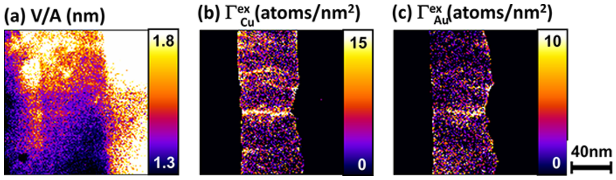

Fig. 2. Additional maps extracted from the thickness and composition maps shown in Fig. 1: (a) V/A map, (b) Cu-enrichment map and (c) Au-enrichment map.

Figure 2 shows the *V*/*A* map (a) determined from Fig. 1, and the Cu- and Au-enrichment maps (b and c), respectively. From the Cu- and Au-enrichment maps, the total excess atoms at the center part of the Ni GB are ∼130 atoms/nm^2 for Cu and 60 atoms/nm^2 for Au. The average number of atoms at a monolayer in the Ni matrix is given as ∼18 atoms/nm^2 per close-packed {111} plane in fcc metals [33]. Therefore, the Cu and Au segregation levels at the Ni boundary are ∼7 and ∼3 monolayers, respectively, and the total amount of segregant atoms becomes ∼10 monolayers for both the Cu and Au co-segregations. Obviously, the segregation levels for Cu and Au in Ni are extremely high in comparison to typical Gibbsian segregation in other alloying systems [34].

Specimen thickness information determined simultaneously with compositions in the ζ-factor method is very useful, as shown above. This approach has also been applied to determine individual elemental volumes of heterostructured nanoparticles in combination with the 3D electron tomography technique [35].

Applications to light element analysis

Soft X-rays with energy <2 keV are significantly absorbed even in a thin specimen. For example, characteristic *K* lines below phosphorus (atomic number 15) and *L* lines below zirconium (atomic number 40) are in this category. Therefore, for quantitative analysis including light elements such as C, N and O, an absorption correction is essential. Figure 3 shows a set of composition maps of yttrium-stabilized zirconia quantified by the ζ-factor method: (i) ADF-STEM image, (ii) Zr map, (iii) Y map, (iv) O map, (v) absorption-loss map for the oxygen *K* line and (vi) thickness map. The thickness in this field of view is low enough (<100 nm) for typical electron microscopy characterization including X-ray analysis. However, the absorption loss for the oxygen *K* line can be as high as 40%. Obviously, without an absorption correction the oxygen composition hardly reaches ∼67 at% as shown in the O map quantified through the ζ-factor method with absorption correction (Fig. 3d). The ζ-factor method was also applied by Fladischer and Grogger [36] to quantify (except for hydrogen) organic semiconducting materials frequently used in organic electronics: $C_{32}H_{16}CuN_8$ and $C_{36}H_{16}N_4O_2$. Although the absorption of X-ray lines from those light elements is significant in these organic systems, the quantified results exhibit substantial agreement with the nominal values expected for all specimens.

Another issue for light element analysis, besides the significant X-ray absorption, is peak overlap. If the energy resolution of an XEDS spectrometer is not sufficient, characteristic X-ray lines in the soft X-ray region are superimposed with one another over uneven backgrounds. Surprisingly, X-ray mapping of those light elements including Be, C and O was performed '60 years ago' at the Cavendish Laboratory, Cambridge University, in the UK by Ray Dolby [37]. At the time, the energy resolution of a gas-based X-ray spectrometer was extremely poor and *K* peaks of Be, C and O were completely superimposed. However, Dolby developed the deconvolution scheme for peak separation and obtained those elemental maps successfully. After Dolby earned his PhD, he applied his experience to sound and founded the famous Dolby Laboratories, where he invented the Dolby noise-reduction system [38].

Nowadays, SDDs have taken over from Si(Li) detectors and are standard in modern S/TEM instruments. The energy resolution of the SDD system can be ∼130 eV or slightly better, which is not significant improvement in comparison to the Si(Li) systems (∼135 eV). However, this minor improvement in the energy resolution at the defined energy for XEDS system, 5.9 keV, provides sufficient enough energy resolutions at the soft X-ray range <2 keV. Thus, the peaks of those light element *K* lines are already separated without any sophisticated peak deconvolution. Quantitative X-ray analysis in S/TEM through the ζ-factor method was applied to silicon hexaboride SiB_6 and boron carbide [39]. Figure 4 shows the B/C ratio quantified by the ζ-factor method, plotted as a function of the specimen thickness. The dashed line indicates the nominal composition ratio (B/C = 4.3) determined by independent combustion gas analysis. Even at the thicker region, ∼250 nm, the B/C ratio is consistent, which means that the significant X-ray absorption for both the light elements was successfully corrected. With careful spectral processing in background subtraction and appropriate absorption correction via the ζ-factor method, light element analysis is successful down to atomic number 5.

ζ-factor as a system sensitivity parameter

As mentioned above, the ζ-factor is related to X-ray generation and detection including the detector solid angle. The ζ-factors can be determined from thin films with known composition and thickness, and from pure element thin films with known thickness [23]. Additionally, an entire set of ζ-factors for *K*-shell X-ray lines can be estimated from a single spectrum [23] generated from the National Institute of Standards and Technology (NIST) thin-film, glass, standard reference material (SRM) 2063 [40] or the re-issued 2063a [41]. Figure 5a compares ζ-factors determined and estimated from the SRM2063a specimen in a 300 keV VG HB 603 dedicated STEM (triangles) and in a 200 keV JEOL JEM-ARM200CF S/TEM with a 100 mm^2 SDD (circles) [42]. The ζ-factor values in JEM-ARM200CF are approximately one-third of those in HB603, which implies that the X-ray collection efficiency in JEM-ARM200CF is approximately three times higher than that in HB603. From the reported value of the X-ray collection angle in the HB603 [43], the collection angle of the 100 mm^2 detector in JEM-ARM200CF was estimated as ∼0.53 sr by taking into account the difference in the ionization cross section at different kV [42]. Later, the position of particular 100 mm^2 SDD was optimized in the JEM-ARM200CF at Lehigh and then the collection angle became ∼0.64 sr. One of the ζ-factor values, e.g. the ζ-factor for the Fe *K* line, can be used as a system parameter

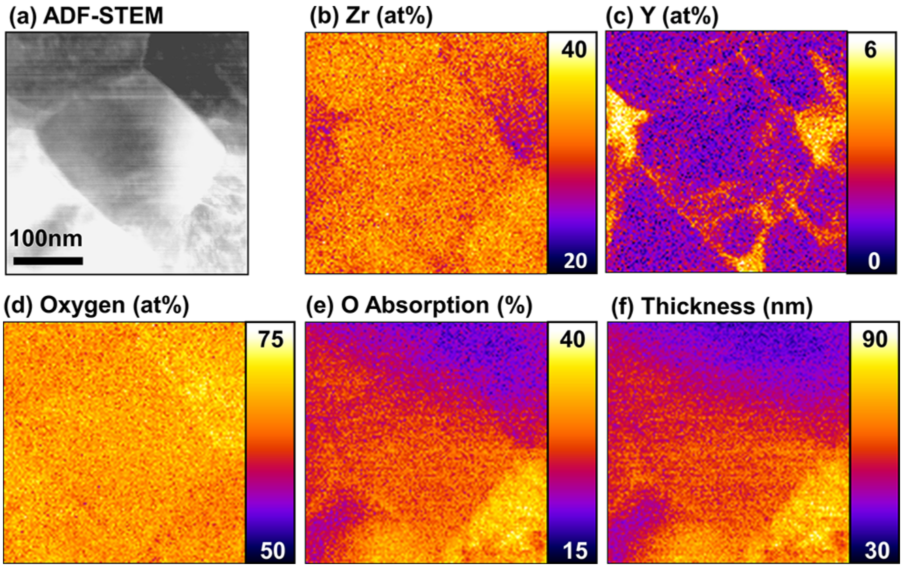

Fig. 3. Summary of X-ray maps from yttrium-stabilized zirconia quantified by the ζ-factor method: (a) ADF-STEM image, (b) Zr map, (c) Y map, (d) O map, (e) absorption-loss map for the oxygen *K* line and (f) thickness map.

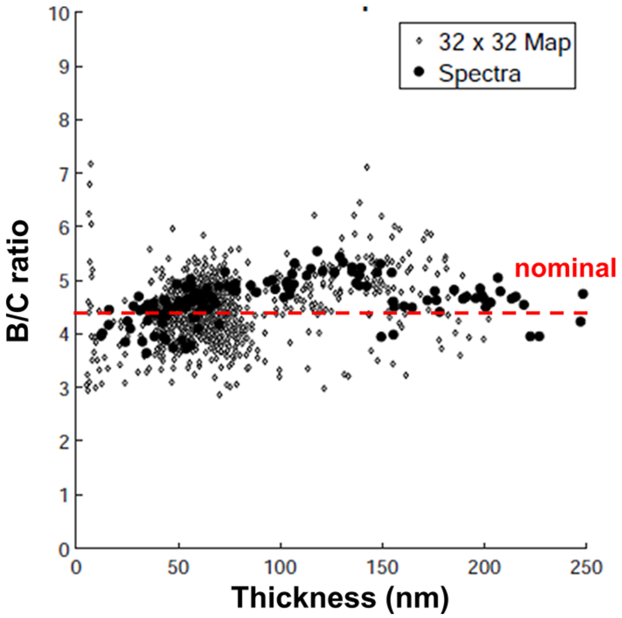

Fig. 4. The Boron/Carbon atomic ratio quantified from a boron carbide specimen by the ζ-factor method, plotted against the specimen thickness [39]. The dashed line indicates the B/C ratio (=4.3) determined by independent combustion gas analysis.

to describe the X-ray collection performance. The lower the ζ-factor value, the higher the X-ray collection efficiency.

In ζ-factor estimation from spectra in SRM2063a, thickness values of the detector window materials can be determined during the ζ-factor estimation [23]. Therefore, using the thickness values of the detector window, the detector efficiency can also be estimated [23]. Figure 5b shows the detector efficiency of the 100 mm^2 SDD system in JEM-ARM200CF calculated from the determined thickness values of detector window materials, plotted as a function of the X-ray energy [42]. It should be mentioned that the decrease in the detector efficiency after ∼10 keV is due to the shorter crystal thickness of the SDD.

There are several advantages to the ζ-factor method over the conventional quantitative approaches. In addition, the ζ-factor method is available in several commercial and non-commercial X-ray analysis packages. More useful information beyond compositions can be obtained through the ζ-factor method.

Progress in spatial resolution of X-ray analysis

Progress in X-ray mapping

Since the first attempt by Peter Duncumb in a house-made electron microscope with a scanning system for acquisition of emitted X-ray signals [44], X-ray mapping became a standard approach and obviously one of the essential characterization tools used widely to extract quantitative information from various materials in SEMs and S/TEMs. It should be noted that these initial demonstrations of X-ray mapping, both by Peter Duncumb and Ray Dolby, were conducted under supervision of Ellis Cosslett '∼60 years ago'. Spatial resolution of X-ray analysis is more significantly improved, down to 1 Å level due to advances of the latest aberration correction technologies. Additionally, development of large solid-angle SDDs and their multiple arrangements also improve poor signal collection efficiency, and hence the analytical sensitivity. By using the aberration-corrected S/TEMs in combination with a larger solid-angle SDD or a set of SDDs, it is possible to obtain atomic-resolution X-ray maps [e.g. 45, 46]. Figure 6 compares the first X-ray map by Duncumb [41] and an atomic-resolution X-ray map measured by the aberration-corrected JEM-ARM200CF S/TEM at Lehigh. Over '60 years', X-ray analysis has reached the ultimate spatial resolution.

Atomic-resolution X-ray mapping in aberration-corrected S/TEMs

Once such atomic-resolution elemental maps as shown in Fig. 6b is obtained in the latest instruments, and an obvious

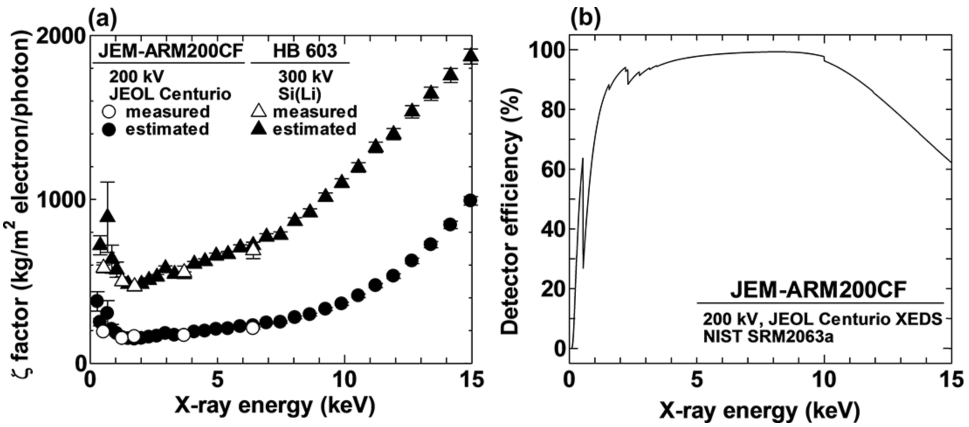

Fig. 5. (a) Comparison of the ζ-factors determined (open symbols) and estimated (closed symbols) using the NIST SRM2063a thin film in VG HB 630 at 300 keV (triangles) and in JEOL JEM-ARM200CF at 200 keV (circles). (b) Detector efficiency of the 100 mm^2 SDD system in JEM-ARM200CF determined after the ζ-factor estimation [42].

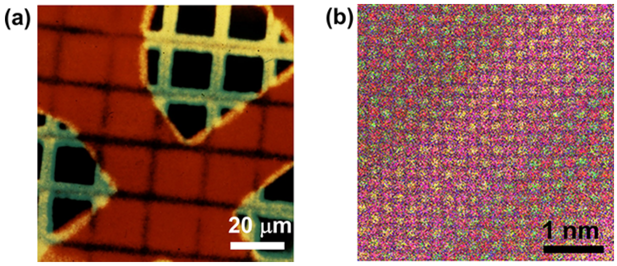

Fig. 6. Comparison of X-ray maps: (a) the first X-ray map of Cu and Ag grids (Cu: red and Ag: yellow) by Duncumb [44] and (b) an atomic-resolution X-ray map of a $SrTiO_3$/$LaMnO_3$ multilayer obtained by the aberration-corrected JEM-ARM200CF AEM at Lehigh (Sr: red, Ti: green, O: blue, La: magenta and Mn: yellow).

next step is to quantify them. Figure 7 shows a set of atomic-resolution X-ray maps acquired from a [001]-projected GaAs thin specimen using an aberration-corrected JEM-ARM200CF equipped with a 100 mm^2 SDD system [45]. In the [001]-projection of GaAs, the Ga and As layers are alternately distributed. Unfortunately, this configuration may not appear clearly in the high-angle annular dark-field (HAADF) STEM image (Fig. 7a) because of the small difference in the atomic number between Ga (31) and As (33). As shown in the elemental maps of (b) Ga and (c) As, with (d) their color overlay, atomic layers of Ga and As are separated as expected. However, in the compositional maps (e: Ga and f: As) quantified by the ζ-factor method, the compositions do not reach 0 or 100 at% in the corresponding atomic layers, as expected from the atom arrangement of the GaAs structure. The maximum and minimum values of measured compositions are ∼70 and 30 at% as shown in the quantified Ga and As maps. The average compositions of whole Ga and As maps are 50.8 and 49.2 at%, respectively, close to the nominal value (50:50). This average composition implies that the quantification procedure itself was performed correctly. The deviation in compositions from the target values (0 or 100 at%) estimated from the structure is partially due to beam broadening. In addition, according to the thickness map (Fig. 7g) determined from measured X-ray intensities by the ζ-factor method, there are relatively large variations: ∼60 and 30 nm at on- and off-column regions, respectively.

In order to understand the composition and thickness differences of on- and off-atomic-column positions, X-ray maps were measured from the [001]-projected GaAs at different thickness regions and quantified. The Ga compositions extracted at the Ga columns, As columns and off-columns are plotted against the specimen thickness in Fig. 8. The concentrations for each type of the atomic columns were determined by averaging 9 (3×3) pixels at the Ga, As and off-columns in individual maps. The error bars represent 3σ (99% confidence limit). In addition, the averaged Ga composition and thickness in individual maps are also plotted in Fig. 8. From this plot, it is evident that (i) the compositions at both atomic columns do not reach 100:0 at% even in the thinnest region but come close to the average composition (50:50 at%) with an increase in the specimen thickness, (ii) the compositions at off-column positions exhibit the compound composition (50:50 at%) within the thickness regions covered in this study, (iii) the average compositions of individual maps also agree well with the compound composition and (iv) the thickness values at off-column positions are lower than those at atomic column positions. The thickness difference between atomic and off-columns are significant in Regions 2 and 3. Both surfaces of the specimen prepared by the ion milling may not be atomically flat. However, it is unlikely that local specimen thickness changes by this magnitude. Since the specimen thickness was determined directly from the Ga Kα and As Kα intensities by the ζ-factor method, this thickness variation between on- and off-atomic columns indicates that abnormal X-ray intensities are emitted at the atomic-column positions due to electron channeling [47]. An atomic-resolution map is usually obtained at a highly symmetric zone axis, in which the incident probe propagation is strongly influenced by the atomic arrangement, i.e. the incident electrons can be channeled and dechannneled at the atomic columns [48]. The dechanneling of incident electrons to other positions induces X-ray signal generations from neighbor columns. Therefore, the dechanneling can be another reason for the deviation in compositions from the target values, as well as regular probe broadening.

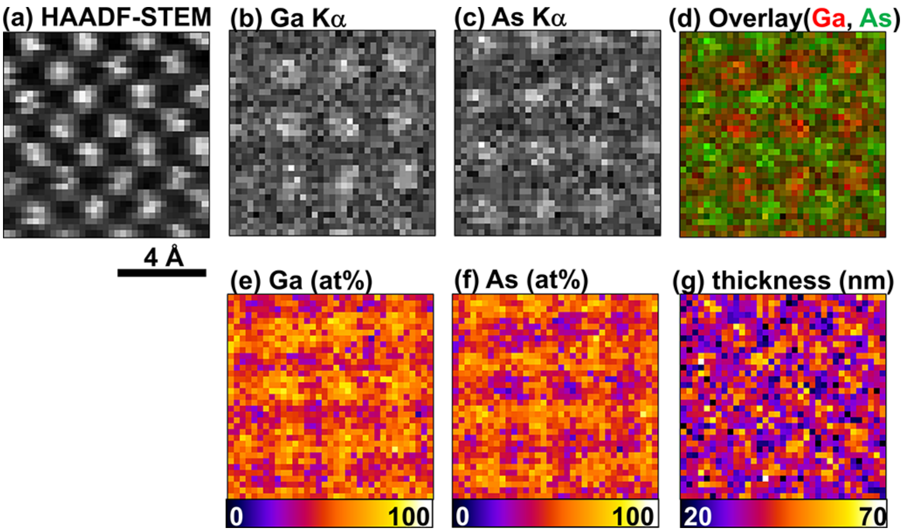

Fig. 7. A set of quantitative X-ray maps from a [100]-projected GaAs specimen: (a) HAADF-STEM image, (b) Ga K intensity, (c) As K intensity, (d) color overlay of Ga K (red) and As K (green), (e) Ga composition, (f) As composition and (g) thickness.

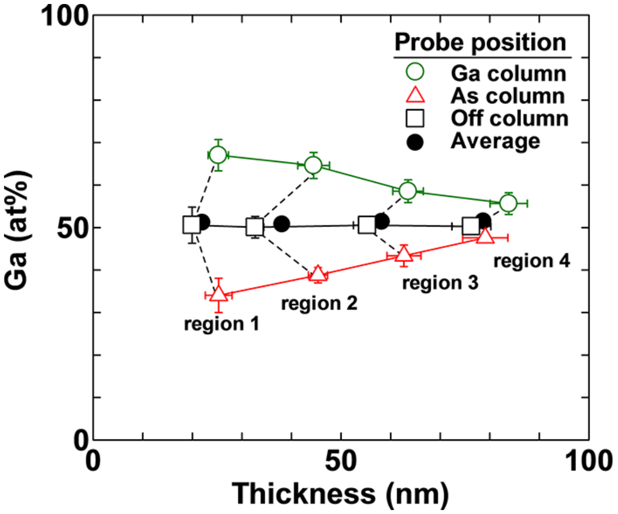

Fig. 8. Ga composition extracted from Ga, As and off-column positions in atomic-resolution X-ray maps of [001]-projected GaAs measured at four different thickness regions, plotted against the specimen thickness. Both the Ga composition and thickness were determined by the ζ-factor method. The average values were determined from whole maps instead of selected positions.

Theoretical evaluation of electron propagation in an oriented crystal

There have been several theoretical attempts to understand the electron channeling behavior in atomic-resolution imaging and chemical analysis. In particular, Forbes et al. [48], Kotula et al. [49], Lu et al. [50], Kothleitner et al. [46], Chen et al. [51] and MacAuthor et al. [52] explored quantification of atomic-resolution X-ray mapping and some employed theoretical simulations to understand abnormal X-ray signal generations caused by electron channeling toward quantification.

In order to understand the abnormal X-ray signal generation in atomic-resolution mapping, it is first necessary to know how the incident electron probe propagates a crystalline material oriented in highly symmetric zone axis. The electron propagation, as an electron wave function, can be simulated by a multislice calculation. In this study, the xHREM code [53] was used to simulate the electron wave function. For the determination of appropriate electron-intensity distributions, the intensity loss (the electron absorption) due to thermal diffuse scattering was taken into account. It should also be noted that typical multislice codes (including the xHREM package) are designed for image simulation, not for chemical analysis, so that any contributions of the electron source size to image formation are not included. In this simulation, the source size contribution was incorporated as the 2D Gaussian distribution based on the gun brightness and then the true electron wave functions were obtained by convoluting the 2D Gaussian intensity distribution with the wave functions simulated through xHREM. For the simulation of true electron wave function, a cold field-emission gun was selected with the probe current of 250 pA, which is a typical probe current for atomic-resolution X-ray mapping in a JEOL JEM-ARM200CF S/TEM. The calculation of the probe current distribution and the convolution process can be found elsewhere [54]. In this calculation of the probe current contribution, the electron gun is assumed as a point source, which is not ideal. However, this effect could be minimized by taking averages of X-ray signals around atomic columns as described in following section.

Figure 9 shows a set of simulated intensity distributions at several different specimen thicknesses when the incident electron probe is located at Ga, As and off-columns in a [001]-projected GaAs crystal. The electron wave functions were simulated up to over 100 nm at the convergent semi-angle of 25 mrad with fully aberration-corrected configurations only including the fifth-order spherical aberration and 6-fold astigmatism, which is reasonable for the CEOS ASCOR corrector in the JEM-ARM200CF S/TEM. Note that one-quarter of the lattice parameter of the GaAs crystal (~0.14 nm) was used as a slice thickness, and hence, over 750 slices were used for the multislice calculation in this study. The contribution of the incident probe current is already convoluted in all the distributions shown in Fig. 9. The electron distribution

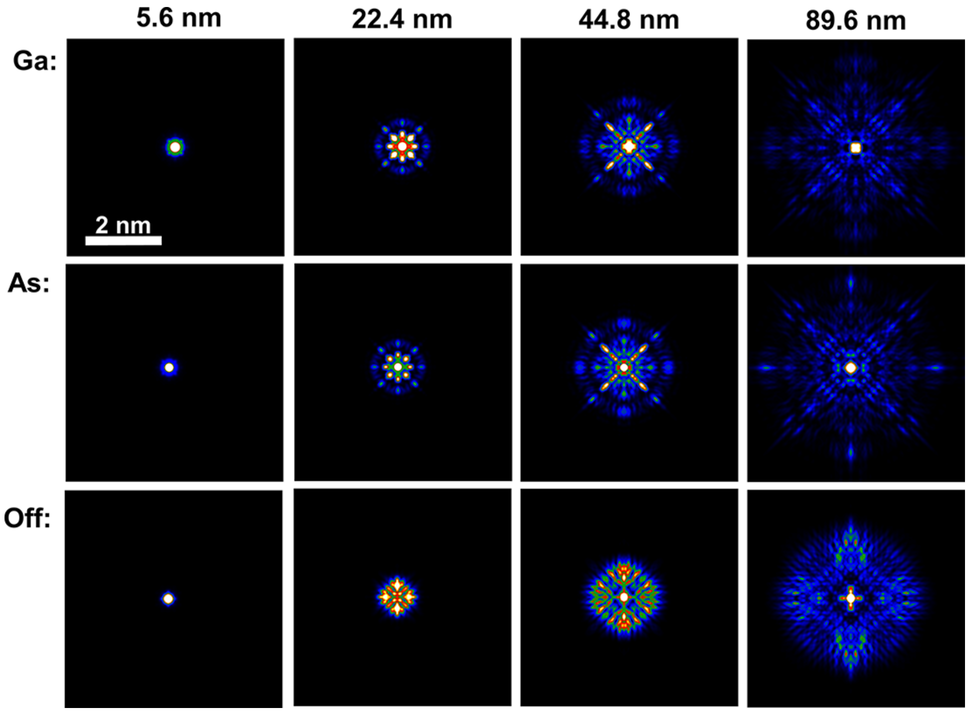

Fig. 9. Simulated intensity distributions several different specimen thicknesses when the incident electron probe is located at Ga, As and off-columns in a [001]-projected GaAs crystal.

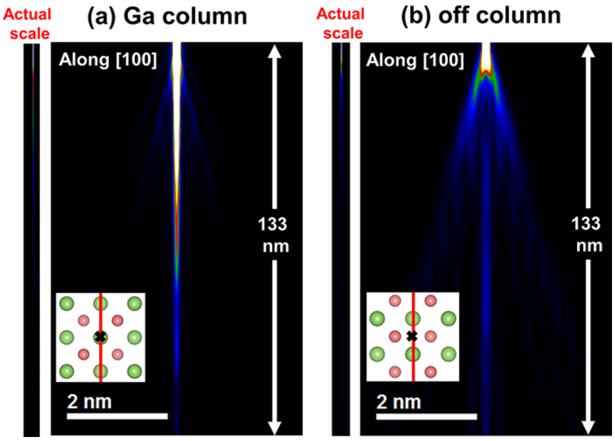

Fig. 10. Vertical views of electron propagations at the (a) Ga and (b) off-columns. The true aspect ratio versions are also shown in the left-hand side.

is not homogeneous but strongly related to atomic arrangements, which are scattering sources. Intensity distributions at the Ga and As columns are very similar. This is because Ga and As have similar atomic numbers and are symmetrically arranged in the [001]-projected GaAs. Conversely, the intensity distributions at the off-column are very different from those at the Ga and As columns. The electron scattering behaviors including distribution area sizes (i.e. spatial resolutions) are strongly dependent on the incident probe nature (size and distribution), the incident probe position and the atomic configuration of a crystal. Therefore, these wave function simulations are essential to understand the interaction between the incident electrons and crystalline materials.

Figure 10 shows vertical views of electron propagations at the (i) Ga and (ii) off-columns. The incident probe position and the vertical section are indicated by a crossmark and a solid line, respectively, in inserted diagrams of the [001]-projected GaAs unit cell (Ga atom: green and As atoms: red). It should be noted that these vertical views are expanded horizontally to display the details of electron scattering behaviors. The vertical views with the true aspect ratio are also inserted in the left-hand side of the main vertical views while keeping the same vertical length (thickness). The electron propagations in a thin specimen occur in extremely narrow ranges. When the incident probe is placed at the Ga column, the electrons seem to remain at the Ga column. Conversely, the incident electrons seem to be diffused into neighbor columns. As expected from the difference in the electron distributions shown in Fig. 9, the electron propagation varies significantly at different incident probe positions.

The electron-distribution diameters can be determined by central-limit integration. Two different diameters, containing 59% and 90% of the incident intensity, were determined at each slice plane. These diameters are typically used for specifying resolution in ADF-STEM imaging [55–57] and for spatial resolution for X-ray analysis [3], respectively. The calculated diameters at (i) the Ga column and (ii) off-column are plotted against the specimen thickness in Fig. 11. The 90% diameters can be treated as the spatial resolution in X-ray analysis and the traditional Gaussian beam-broadening model [58] is also plotted in Fig. 11 for comparison. The diameters determined from the electron wave functions exhibit an approximately linear relationship with thickness. The 59% diameter at the Ga column is smaller than that at the off-column up to a thickness of 70 nm and then the 59% diameters both at the Ga and off-columns become similar. Conversely, the 90%

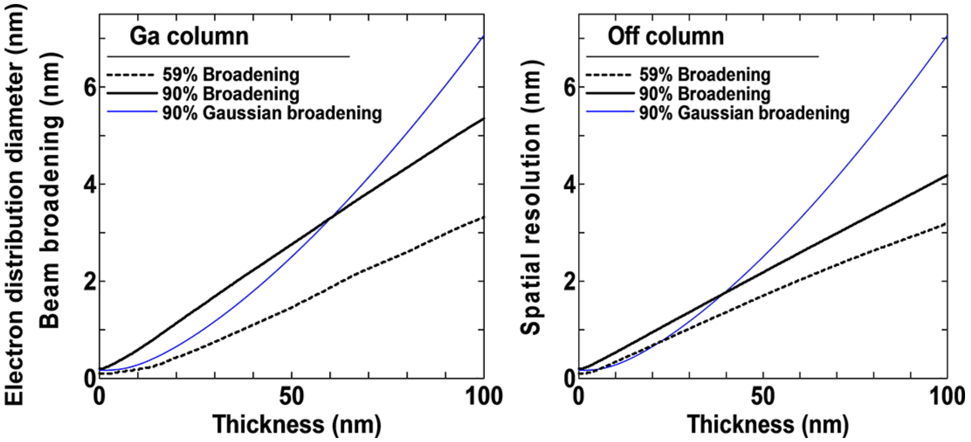

Fig. 11. The intensity distribution diameters, which contain 59% and 90% of the incident intensity, respectively, at (a) the Ga and (b) off-columns determined by central-limit integration, plotted as a function of the specimen thickness. The dashed lines indicate the traditional Gaussian beam-broadening model, which contains 90% of the total intensity [58].

diameter at the Ga column position is larger than that at the off-column within the thickness range in this simulation. The opposite thickness dependence between the central and outer portions is rather confusing. However, it can be seen that the central part of the electron distribution exhibits more electron channeling and the outer part of electron distribution mainly results from atomic scattering. The thickness dependence of the Gaussian broadening model is not linear: the diameter increases as $\sim t^{3/2}$. The discrepancy between the Gaussian broadening model and the electron wave functions is mainly due to the neglect of electron channeling and the probe convergence angle. Although the Gaussian broadening model is useful to predict the analytical spatial resolution for amorphous materials and randomly oriented crystalline materials, an appropriate wave function calculation is essential for estimating the spatial resolution in crystalline specimens oriented to a high symmetrical zone axis for atomic-resolution analysis.

Simulation of atomic-resolution X-ray mapping

Once the electron distributions are simulated as shown in Figs. 9 and 10, X-ray signals can be evaluated at each sliced plane. X-ray spectra were simulated at individual sliced layers by porting the X-ray generation engine of the legacy Desktop Spectrum Analyzer codes [59]. For the X-ray simulation, the detector geometry and configurations of the JEM-ARM200CF with a single 100 mm^2 SDD system were used. An X-ray spectrum at a certain depth from the top surface of the specimen was obtained by adding individual spectra. In this spectral simulation, X-ray absorption and detector efficiency were also taken into account.

The GaAs unit cell was divided by 21 × 21 pixels and X-ray spectra were simulated at individual pixels in the unit cell and at different thickness. Then, Ga Kα and As Kα maps were constructed by extracting characteristic X-ray intensities of the Ga Kα and As Kα lines after background subtraction. Figure 12 shows a set of simulated results summarized for different specimen thicknesses of 5.6, 22.4, 44.8 and 89.6 nm: simulated HAADF-STEM images in top row, simulated ratio maps of Ga Kα to total Kα intensity (sum of Ga Kα and As Kα) in middle row and maps of the total K intensity normalized by the averaged total K intensity in bottom row. Because X-ray generation and detection for the Ga Kα and As Kα lines are very similar due to close atomic numbers of Ga (31) and As (33), the maps of Ga Kα/total Kα intensity ratio (Ga intensity ratio) approximately indicate the Ga concentration fraction. Although the individual atomic columns are still separated in the Ga intensity ratio maps even at thicker region, more mixing can be seen in generated X-ray signals between atomic columns as the specimen thickness increases. The ratio of the total Kα intensity over the averaged total Kα intensity, i.e. the relative total Kα intensity, shown in the bottom row in Fig. 12 exhibits the abnormal X-ray generation at atomic-column positions, which indicates electron channeling. The difference in the relative total Kα intensity between on- and off-atomic columns is very high (nearly twice) but the difference is reduced as the specimen thickness increases.

Because the Ga intensity ratio (maps in the middle row in Fig. 12) can be treated as a Ga concentration fraction, the values at the Ga, As and off-columns are extracted in the maps and plotted against the specimen thickness in Fig. 13. This plot is essentially equivalent to the measured Ga compositions plotted against the specimen thickness (Fig. 8). As expected from the quantified results, the simulated Ga intensity ratio at the off-column is ∼0.5 within the thickness range in this simulation except thinner regions than 10 nm. The Ga intensity ratios at Ga and As columns show very similar thickness dependence to the measured Ga composition shown in Fig. 8. It is still very challenging to determine true atom distributions from the atomic-resolution X-ray maps by considering the electron channeling behaviors. However, attempts of quantification of these atomic-resolution maps will offer true atomic configurations at the atomic scale if an appropriate modeling and a correction scheme for electron channeling are established.

Optimization of instrument conditions for the best spatial resolution in atomic-resolution X-ray mapping

Obviously, the aberration correction has brought further flexibility in instrumental conditions for imaging and analysis and it is very important to configure those operating conditions to achieve the best possible spatial resolution in analysis. This section explores the optimum instrumental conditions in terms of (i) the convergence semi-angle (α) and (ii)

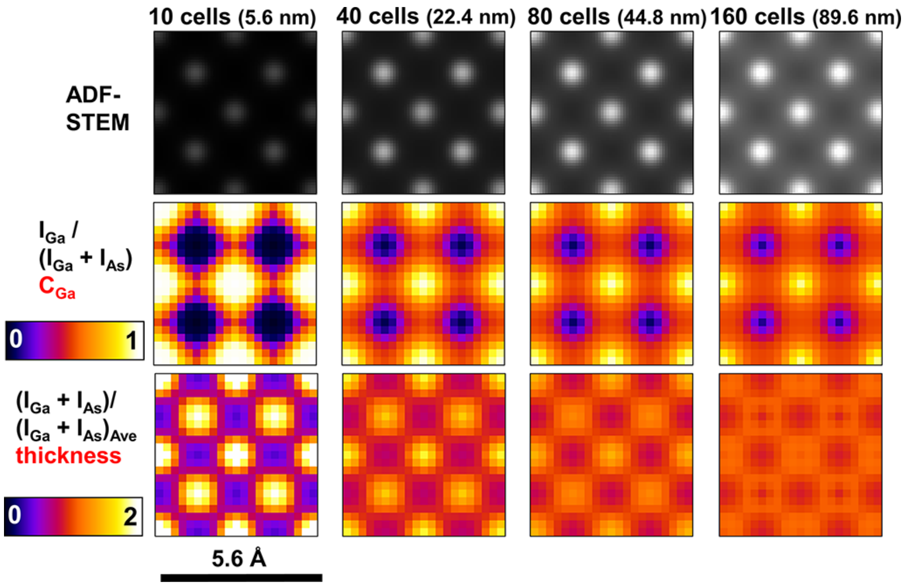

Fig. 12. A set of simulated HAADF images (top), ratio maps of Ga K over total K intensities (middle), and normalized total K intensity maps (bottom) at different thicknesses.

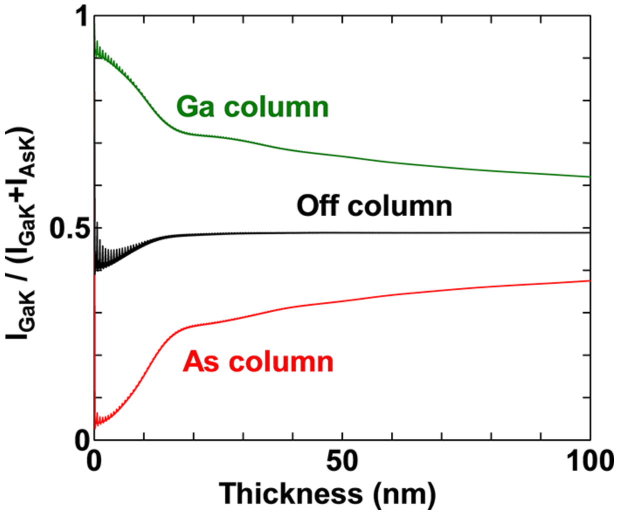

Fig. 13. The ratio of the Ga Kα intensity over total Kα intensity at the Ga, As and off-columns are extracted in the maps, plotted against the specimen thickness.

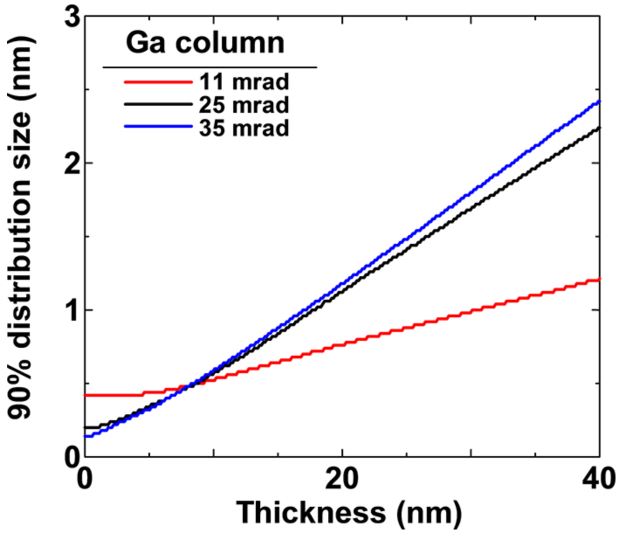

Fig. 14. Comparison of the 90% intensity distribution diameters at the Ga column at the convergence semi-angle (α) of 11, 25 and 35 mrad.

the defocus for the best spatial resolution in atomic-column X-ray analysis by using the theoretical approach described above.

To evaluate the best convergence semi-angle, the simulation was performed for the [001]-projected GaAs thin specimen with the probe current of 250 pA at the convergence semi-angle (α) of 11, 25 and 35 mrad. Note that results at 25 and 35 mrad are under aberration correction but not at 11 mrad, and the incident probe size decreases as α increases. The 90% intensity distribution sizes at the Ga column were determined for three convergence angle conditions by the central-limit integral and plotted against the specimen thickness in Fig. 14. At very thin region up to ~10 nm, the smallest distribution size can be obtained at $\alpha = 35$ mrad. However, with an increase in the specimen thickness, the distribution size is less at lower α. So, higher convergence angles offered by the aberration correction enhance the distribution size at thicker regions.

Figure 15 shows a set of the Ga intensity ratio maps (the Ga Kα intensity over sum of the Ga Kα and As Kα intensities) of the [001]-projected GaAs unit cell at different α and different specimen thicknesses. The maps at $\alpha = 11$ mrad show poor resolution and the Ga ratio does not reach 0 and 1 at the As and Ga positions, respectively. Obviously, the finer incident probe size, i.e. the aberration correction really matters to achieve atomic resolution even though the 90% distribution size is less at thicker regions. In the aberration-corrected

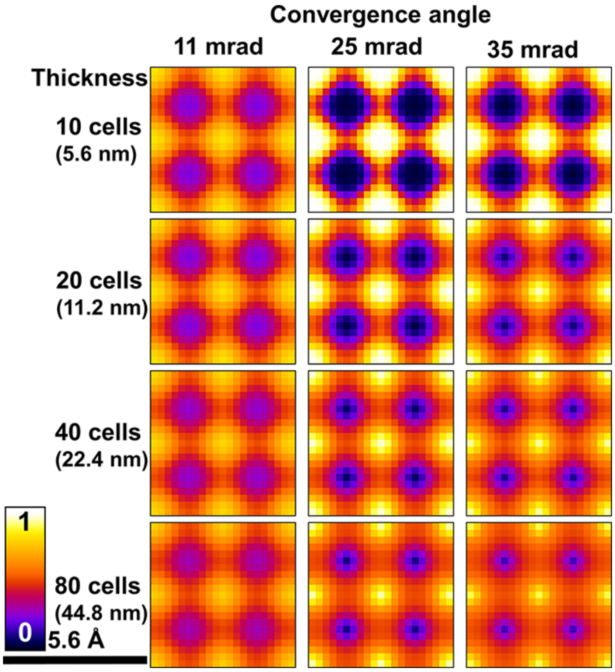

Fig. 15. A set of the Ga ratio maps of the [001]-projected GaAs unit cell, summarized at different α and the different specimen thicknesses.

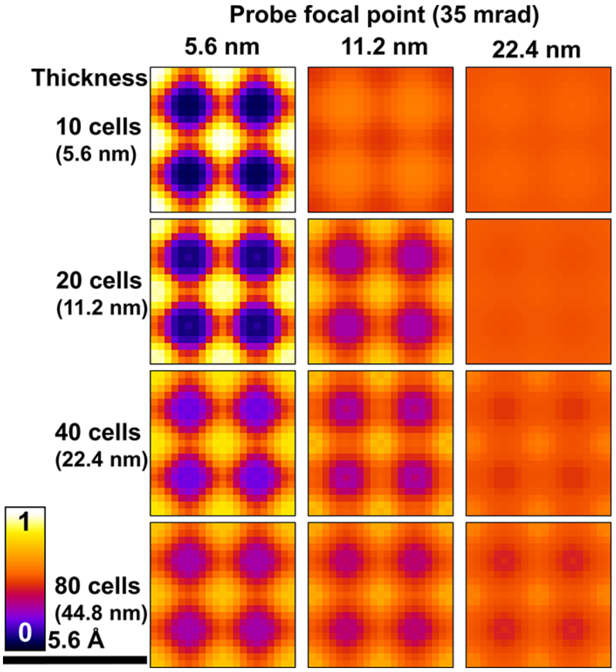

Fig. 16. A set of the Ga ratio maps of the [001]-projected GaAs unit cell, simulated at $\alpha = 35$ mrad and the different focal position.

conditions at $\alpha = 25$ and 35 mrad, superior resolution can be obtained up to the 40-nm-thick specimen. As the specimen thickness is very thin (~5 nm), the Ga ratio reaches 0 and 1 at the As and Ga positions, respectively, both at $\alpha = 25$ and 35 mrad. However, the resolution of the Ga ratio map is better at $\alpha = 25$ mrad when thicker specimens are analyzed. The simulated results suggest that the convergence angle of 25 mrad in the aberration-corrected condition would provide better spatial resolution unless the specimen thickness is very thin (<5 nm for the GaAs crystal at 200 keV).

All the simulated X-ray maps shown above are in the conditions that the incident probe is focused on the top surface (incident probe side). Figure 16 shows a set of the Ga ratio maps at $\alpha = 35$ mrad simulated with three different focal points. These focal points are shifted to inside of the specimen (i.e. underfocus). When the defocus step is small, then better spatial resolution is maintained. However, in general, the defocus degrades the spatial resolution significantly. Therefore, the focal point should be kept at the top surface, i.e. the focal position for the best HAADF-STEM imaging. It should also be mentioned that these optimized conditions for X-ray analysis should be applicable to EELS analysis as well.

Progress in sensitivity of X-ray analysis

Characterization of single atoms in materials

Identification of individual atoms randomly distributed in materials, specification of their locations in terms of their microstructure and quantification, i.e. total characterizations of single atoms, are the ultimate goal of any chemical analysis. To perform the single-atom characterization, atomic-scale spatial resolution is required as well as single-atom detection sensitivity. In fact, some of fundamental materials problems such as phase transformations and dopant segregation on defects and interfaces might be controlled by a few atoms within a few atomic layers. Thus, single-atom characterization/analysis is essential for further understanding of such phenomena and for advanced materials developments. Since the latest aberration correction technology for STEMs offers more probe current while maintaining refined probe sizes, both spatial resolution and sensitivity for imaging/analysis can also be significantly improved and atomic-resolution elemental mapping is now regularly carried out by both EELS and XEDS as mentioned above.

Imaging single atoms in a thin specimen is now possible by using aberration-corrected STEM instruments. For example, detailed Bismuth (Bi) segregation behaviors in Cu were characterized by STEM imaging [60]. Bi has long been known to severely degrade the mechanical properties of Cu by segregating on GBs. Since the mechanisms behind this GB embrittlement due to the Bi segregation are not well understood, it is important to find out individual Bi-atom locations around Cu GBs. Figure 17 shows a HAADF-STEM image of a Bi-doped twist GB in Cu (left). Fast Fourier transformation (FFT) filtering was applied to the selected region in the image to enhance visibility of individual Bi-atom locations as well as the extra half planes of edge dislocations. The atomic arrangements are schematically shown in both the filtered and raw HAADF images. In this image it can be seen that the large Bi atoms that have segregated to the GB exist near the dislocation cores of the edge dislocations inhabiting the GB [60].

X-ray analysis of single atoms in materials

In comparison to STEM imaging, single-atom analysis by EELS and XEDS is still very challenging even by using the aberration-corrected STEMs because signal generation is extremely limited from much smaller analyzed

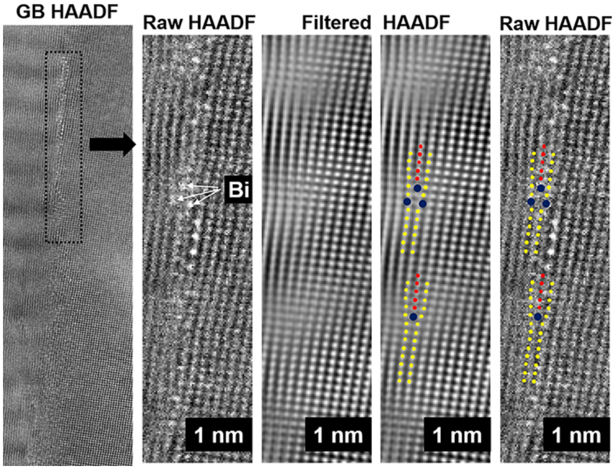

Fig. 17. A HAADF-STEM image of a Bi-doped Cu GB (left). The boxed region was processed through FFT filtering to show individual Bi atoms and GB atomic arrangements [60].

volumes improved by the aberration correction and signal collection is still poor. However, single-atom analysis has been demonstrated in EELS [e.g. 61–64] because of relatively higher signal collection efficiency. As mentioned above, the signal collection efficiency has been dramatically improved by incorporating a large solid-angle SDD or multiple SDDs, and hence single-atom analysis by XEDS was demonstrated in an aberration-corrected STEM [65,66].

In X-ray analysis, elements can be categorized depending on their amounts in materials as follows [2]:

- Major elements: over 10 wt%
- Minor elements: 1–10 wt%
- Trace elements: <1.0 wt%

Obviously, single atoms in electron transparent thin specimens are trace levels and expected signals from single atoms are very low. Using the scheme to simulate atomic-resolution X-ray maps described above, X-ray spectra were simulated for evaluating single-atom analysis.

In GaAs, phosphorus (P) is a well-known impurity element and usually occupies an As site by substitution, and hence GaAs and P are chosen as the host and impurity to evaluate X-ray detectability from a single atom in a crystalline material. Electron wave functions were simulated for three different single P atom positions: top (incident beam side), middle and bottom of a thin specimen, as shown schematically in Fig. 18, and then the X-ray spectra from the P-doped GaAs specimen were simulated.

Figure 19 compares simulated P *K* maps of [001]-projected GaAs thin specimens with different thicknesses of 5.6 nm (10 unit-cell thick), 11.2 nm (20 unit-cell thick) and 22.4 nm (40 unit-cell thick). The calculation was performed for the JEM-ARM200CF at 200 keV with the probe current of 250 pA and the convergence semi-angle of 35 mrad. The single P atom is positioned on an As site near the top surface, middle and bottom of the specimen, respectively, which are indicated at the left-bottom corner in each map (top surface is 0 nm). For this simulation, the incident probe is focused at the top of the specimen as shown in Fig. 18. If specimens are very thin, e.g. 5.6 nm, the P *K* signals can be seen even if the P atom is located in GaAs specimen as shown in Fig. 19. However, for thicker specimens, the P *K* signals are hardly observable unless the P atom is located at the top of the specimen. Therefore, single atoms located on the top surface might be detectable by X-ray analysis.

Another set of simulations was performed for the single-atom detection in the same conditions as the previous calculation shown in Fig. 18. The single P atom positions remain the same as the previous simulation but the probe focal points were shifted from the top surface to the middle and the bottom of the specimen. Figure 20 shows another set of simulated P *K* maps are summarized with respect to different focal points (top, middle and bottom) in a 22.4-nm-thick (=40 unit-cell thick) [001]-projected GaAs specimen.

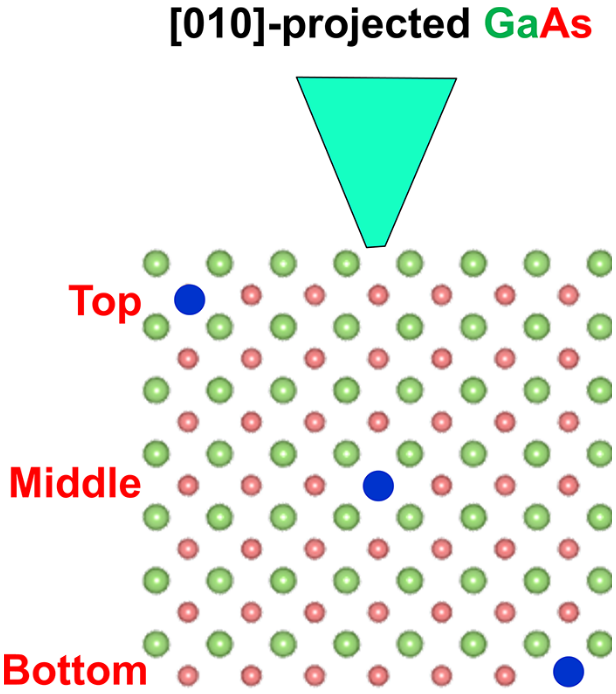

Fig. 18. A schematic diagram of single P atom positions (near top, middle and bottom) in a thin GaAs specimen.

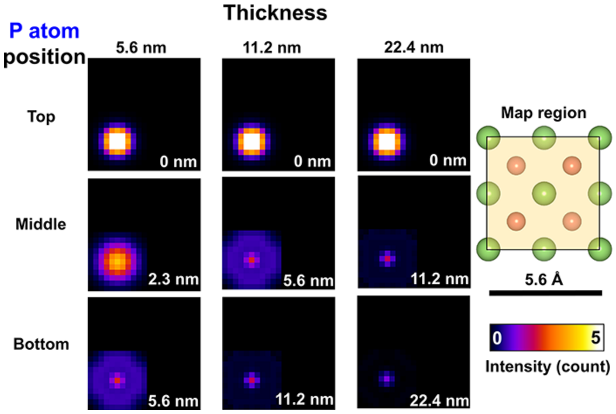

Fig. 19. A set of P *K* maps summarized as a function of the P atom position (top, middle and bottom) at different thick GaAs films, simulated for the JEM-ARM200CF at 200 keV with the probe current of 250 pA and the convergence semi-angle of 35 mrad.

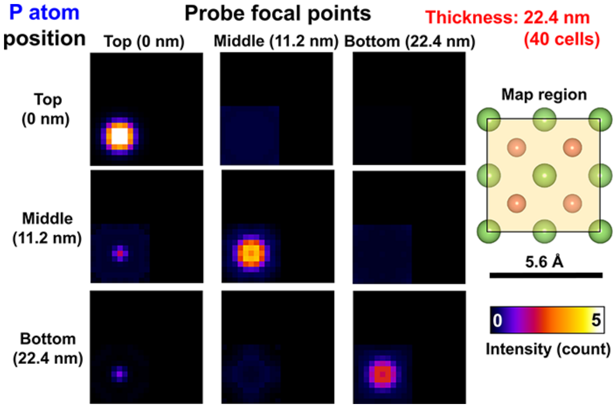

Fig. 20. A set of P *K* maps summarized as a function of the probe focal point (top, middle and bottom of the specimen) and of the P atom position (top, middle and bottom), simulated for the JEM-ARM200CF at 200 keV with the probe current of 250 pA and the convergence semi-angle of 35 mrad.

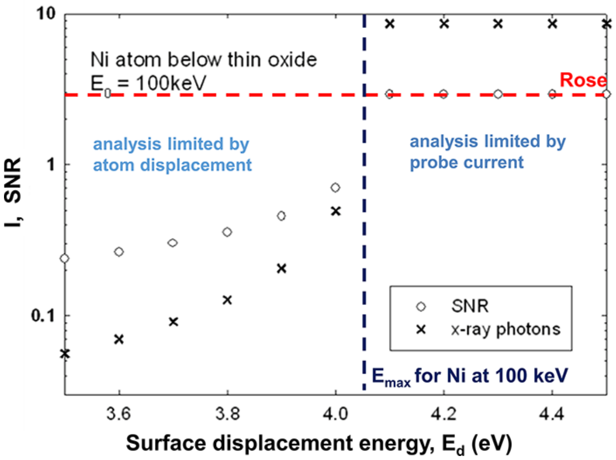

Fig. 21. Number of X-ray photons emitted by a single Ni atom, i.e. the intensity *I*, and its SNR, as a function of the atomic binding energy E_d. The atom is assumed to lie on the beam-exit surface of the specimen. For $E_d > E_{max} \sim 4.1$ eV, an atom dwell time is assumed 1 s with the current density of 10^5 A/cm^2 (e.g. 0.1 nA probe current and 0.3 nm probe diameter) [70].

As shown in Fig. 19, the single P atom at the top surface is detectable by adjusting the probe focus to the top surface. Conversely, the detectability of the P *K* signal is significantly improved by tuning the probe focal points to the specific P atom positions if the high convergence semi-angle is used, e.g. $\alpha = 35$ mrad. This result is very interesting because spatial resolution of X-rays is degraded by defocusing as shown in Fig. 16. This simulation result raises the possibility of obtaining 3D impurity distributions through spectrometry-based techniques (including EELS) by applying through-focus signal acquisition in aberration-corrected STEMs, similar to the through-focus STEM imaging shown in Fig. 17.

Fundamental limits of single-atom analysis

The simulation results above indicate the feasibility of the single-atom detection through XEDS. However, such measurements are still very challenging in practice, so the experimental conditions need to be optimized. As described below, calculations indicate that an important parameter is the microscope accelerating voltage, which should be chosen to be as low as possible, consistent with adequate resolution.

In addition to the limited signals from single atoms, atom displacement under the electron irradiation during signal acquisition could frustrate signal detection from single atoms. Atoms on top of support materials such as catalysis or on a carbon films could easily be very mobile under the electron beam, even though these surface atoms may be more detectable than others embedded in materials as predicted above.

In general, the atomic displacement is avoided if the binding energy of the atom E_d exceeds the maximum energy transfer *Emax* from the primary electron, whose value is given by relativistic kinematics [67]. Detectability of the peak is then determined by its signal/noise ratio, for example using the Rose criterion for a spectrum (signal-to-noise ratio, SNR > 3) [68,69]. The Poisson statistical noise is approximately $(I+B)^{1/2}$ (I and B are the peak intensity count above background and the background count, respectively), giving $SNR = I/(I+B)^{1/2}$, which has been evaluated in Fig. 21 for a single Ni atom on a support film through the Ni Kα line by taking $De = 6 \times 10^{27}$ e/m^2 (for example, 0.1 nA probe current, 0.3 nm probe diameter and 1 s dwell time) [70]. In this example, the Ni atom would just be identifiable ($SNR \sim 3$) when $E_d >$ Emax. Although most of the bremsstrahlung come from the substrate (assumed to contain ∼60 atoms of mean atomic number 10), $B \ll I$ for a reasonable thin support and a small-diameter probe. The value of E_d will depend on the atomic site of the atom, so some atoms may be detectable and others not. Ejection may be less efficient if the atom lies on the beam-entrance surface of the specimen. E_d is certainly lower for momentum transfer 'along' the surface (adatom motion rather than surface sputtering) but the maximum energy available is a factor of 2–4 lower [71]. In all cases, *Emax* is roughly proportional to the incident energy E_0, so use of low-beam energy could be important. Recent XEDS identifications of single Er [72] and Pt [65] atoms used an accelerating voltage of 60 kV. EELS may be the preferable technique for identifying certain elements due to its greater signal collection efficiency [71].

Summary

In this paper, recent progress related to X-ray analysis in S/TEM instruments has been explored in terms of quantitative analysis, spatial resolution and analytical sensitivity. By using the latest aberration-corrected S/TEM instrument with the multiple SDD spectrometer array system, the spatial resolution of analysis reaches down to the atomic levels and the single-atom analysis can be achieved. The various new SDD geometries to improve the detection efficiency also offer superior counting statistics, and hence quantitative X-ray analysis can be performed with high accuracy and precision. Furthermore, the improved energy resolution in the latest SDD system allows researchers to detect X-ray peaks from light elements and to quantify them with improved quantification schemes such as the ζ-factor method.

As a summary, Fig. 22 shows the relationship between the spatial resolution and analytical sensitivity in terms of minimum mass fraction (MMF) of electron-probe instruments. This figure is updated from the previous version published '∼20 years ago' [73], which was modified from original plot

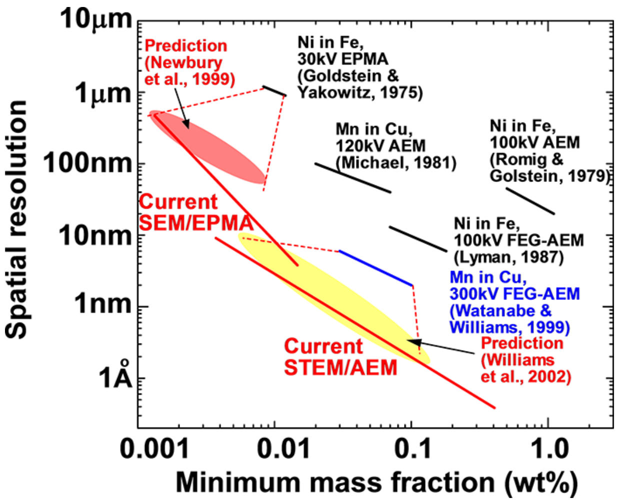

Fig. 22. A summary of the relationship between the spatial resolution and the MMF for the X-ray microanalysis in several electron-probe instruments, updated from the previous version [73] with the latest data. The two shadowed areas were predicted ∼20 years ago for SEM/EPMA- and STEM/AEM-based instruments, respectively. The solid lines below these shadowed areas indicate the current analytical performances in the latest SEM/EPMA and the latest aberration-corrected STEM/AEM.

by Lyman [74]. There are two shadowed areas in this figure: the area in the left-hand side exhibits the predictions of next-generation SEM/EPMA-based X-ray analysis by Newbury et al. [75] and the area in the right-hand side indicates the prediction of X-ray analysis in aberration-corrected STEM [73]. Both were predicted '∼20 years ago' when the aberration correctors and SDDs were not available even in major electron microscopy facilities. The solid lines below these shadowed areas indicate the current analytical performances in the latest SEM/EPMA and the latest aberration-corrected STEM/AEM, respectively. The analytical performances with respect to spatial resolution and MMF have already exceeded the predictions in the modern electron-probe instruments. The latest aberration-corrected STEM with superior X-ray and EELS analysis capability can be regarded as 'Electron Probe Atomic Analyzer', exceeding the Electron Probe Ångstrom Analyzer defined previously [73].

It is our great pleasure to contribute this paper to the 70th anniversary issue of *Microscopy*, which is the Platinum anniversary. With various advances in instrumentations and methodology by researchers, the microscopy field is even getting stronger toward the Diamond anniversary!

Funding

The author M.W. wishes to acknowledge financial support from the National Science Foundation through the grants DMR-2018683 and CMMI-2016279.

Acknowledgements

The authors wish to thank the following scientists for collaboration and discussion: Prof. David B. Williams, Prof. Chis J. Kiely, Mr. David Ackland, Dr. Robert Keyse, Mr. William Mushock, Dr. C. Austin Wade, Dr. Hidetaka Sawada, Dr. Eiji Okunishi, Mr. Masahiko Kanno, Dr. Masaki Morita, Mr. Akira Yasuhara and Dr. Peter Duncumb.

Conflict of Interest

The author declare that they have no conflict of interest.

References

1. Castaing R (1952) [Submitted 1951]. Application des sondes électroniques à une méthode d'analyse ponctuelle chimique et cristallographique: publication ONERA (Office national d'études et de recherches aéronautiques/ Institute for Aeronautical Research) N. 55 (PhD Thesis). (University of Paris, Paris), English translated version is available at http://www.microbeamanalysis.org/history/Castaing-Thesis-clearscan.pdf.
2. Goldstein J I, Newbury D E, Michael J R, Ritchie N W M, Scott J H J, and Joy D C (2018) *Scanning Electron Microscopy and X-ray Microanalysis*. *Fourth edition*, (Springer, New York).
3. Williams D B and Carter C B (2009) *Transmission Electron Microscopy: A Textbook for Materials Science*. *Second edition*, (Springer, New York).
4. Erni R, Rossel M D, Kisielowski C, and Dahmen U (2009) Atomic-resolution imaging with a Sub-50-pm Electron Probe. *Phys. Rev. Lett.* 102: 4.
5. Sawada H, Tanishiro Y, Ohashi N, Tomita T, Hosokawa F, Kaneyama T, Kondo Y, and Takayanagi K (2009) STEM imaging of 47-pm-separated atomic columns by a spherical aberration-corrected electron microscope with a 300-kV cold field emission gun. *J. Electron Microsc.* 58: 357–361.
6. Batson P E (1995) Conduction bandstructure in strained silicon by spatially resolved electron energy loss spectroscopy. *Ultramicroscopy* 59: 63–70.
7. Browning N D and Pennycook S J (1995) Atomic-resolution electron energy-loss spectroscopy in the scanning transmission electron microscope. *J. Microsc.* 180: 230–237.
8. Varela M, Lupini A R, van Benthem K, Borisevich A Y, Chisholm M F, Shibata N, Abe E, and Pennycook S J (2005) Materials characterization in the aberration- corrected scanning transmission electron microscope. *Annu. Rev. Mater. Res.* 35: 539–569.
9. Kimoto K, Asaka T, Nagai T, Saito M, Matsui Y, and Ishizuka K (2007) Element- selective imaging of atomic columns in a crystal using STEM and EELS. *Nature* 450: 702–704.
10. Bosman M, Keast V J, García-Muñoz J L, D'Alfonso A J, Findlay S D, and Allen L J (2007) Two-dimensional mapping of chemical information at atomic resolution. *Phys. Rev. Lett.* 99: 086102.
11. Muller D A, Fitting-Kourkoutis L, Murfitt M, Song J H, Wang H Y, Silcox J, Dellby N, and Krivanek O L (2008) Atomic-scale chemical imaging of composition and bonding by aberration-corrected microscopy. *Science* 319: 1073–1076.
12. Varela M, Oxley M P, Luo W, Tao J, Watanabe M, Lupini A R, Pantelides S T, and Pennycook S J (2009) Atomic resolution imaging of oxidation states in manganites. *Phys. Rev. B* 79: 085117.
13. Watanabe M, Kanno M, and Okunishi E (2010) Atomic-resolution elemental mapping by EELS and XEDS in aberration corrected STEM. *JEOL News* 45: 8–15.
14. Watanabe M, Ackland D W, Burrows A, Kiely C J, Williams D B, Krivanek O L, Dellby N, Murfitt M F, and Szilagyi Z (2006) Improvements of X-ray analytical capabilities by spherical aberration correction in scanning transmission electron microscopy. *Microsc. Microanal.* 12: 515–526.

15. Kotula P G, Michael J R, and Rohde M (2009) Results from two four-channel Si- drift detectors on an SEM: conventional and annular geometries. *Microsc. Microanal.* 15: 116–117.
16. Zaluzec N J (2009) Innovative instrumentation for analysis of nanoparticles: the π steradian detector. *Micros. Today* 17: 56–59.
17. von Harrach H S, Dona P, Freitag B, Soltau H, Niculae A, and Rohde M (2009) An integrated silicon drift detector system for FEI schottky field emission transmission electron microscopes. *Microsc. Microanal.* 15: 208–209.
18. Ohnishi I, Okunishi E, Yamazaki K, Aota N, Miyatake K, Nakanishi M, Ohkura Y, Kondo Y, Yasunaga K, Toh S, and Matsumura S (2011) Development of a large solid angle SDD for TEM and its applications. *Microsc. Microana.* 17. Late Breaking 22.
19. Watanabe M, Sasaki T, Jimbo Y, Okunishi E, and Sawada H (2015) Practical measurement of X-ray detection performance of large-angle silicon drift detectors toward quantitative analysis in the newly developed 300 kV Aberration-Corrected Grand ARM. *Microsc. Microanal.* 21: 1223–1224.
20. Zaluzec N J (2021) First Light on the Argonne PicoProbe and the X-ray Perimeter Array Detector (XPAD). *Microsc. Microanal.* 27: 2070–2074.
21. Cliff G and Lorimer G W (1995) The quantitative analysis of thin specimens. *J. Microsc.* 103: 203–207.
22. Goldstein J I, Costley J L, Lorimer G W, and Reed R J B (1977) Quantitative X-ray analysis in the electron microscopein. In: Johari O (ed.), *Scanning Electron Microscopy – 1977*, Vol. 1, pp 315–324 (IITRI, Chicago, IL).
23. Watanabe M and Williams D B (2006) The quantitative analysis of thin specimens: a review of progress from the cliff-lorimer to the new ζ-factor methods. *J. Microsc.* 221: 89–109.
24. Watanabe M, Horita Z, and Nemoto M (1996) Absorption correction and thickness determination using ζ factor in quantitative X-ray microanalysis. *Ultramicroscopy* 65: 187–198.
25. Watanabe M and Williams D B (2003) Quantification of elemental segregation to lath and grain boundaries in low-alloy steel by STEM X-ray mapping combined with the ζ- factor method. *Z. Metallk.* 94: 307–316.
26. Philibert J (1963) A method for calculating the absorption correction in electron- probe microanalysis. In: Pattee H H, Cosslett V E, and Engström A (eds), *Proceeding 3rd International Congress X-ray Optics and Microanalysis*, pp 379–392 (Academic Press, New York, NY).
27. Falke M, Kraxner J, Terborg R, Kothleitner G, and Grogger W (2018) Composition and thickness mapping using STEM EDS. *Microsc. Microanal.* 24: 764–765.
28. Morita M and Onishi I (2018) Comparing quantitative results of zeta factor method using various values of ionization cross-sections. *Microsc. Microanal.* 24: 770–771.
29. Ritchie N W M NIST DTSA-II, a public domain software package available from the National Institute of Standards and Technology Gaithersburg, MD through http://www.cstl.nist.gov/div837/837.02/epq/dtsa2/index.html.
30. MacArthur K E, Slater T J A, Haigh S J, Ozkaya D, Nellist P D, and Lozano-Perez S (2016) Quantitative energy-dispersive X-ray analysis of catalyst nanoparticles using a partial cross section approach. *Microsc. Microanal.* 22: 71–81.
31. Danylenko M I, Watanabe M, Li C, Krajnikov A V, Williams D B, and Vasiliev M A (2003) Analytical electron microscopy and auger electron spectroscopy study of low- temperature diffusion in multilayer Cr-Cu-Ni-Au thin films. *Thin Solid Films* 444: 75–84.
32. Van Cappellen E and Schmitz A (1992) A simple spot-size versus pixel-size criterion for X-ray microanalysis of thin foils. *Ultramicroscopy* 41: 193–199.
33. Alber U, Müllejans H, and Rühle M (1997) Improved quantification of grain boundary segregation by EDS in a dedicated STEM. *Ultramicroscopy* 69: 105–116.
34. Hondros E D and Seah M P (1977) Segregation to interfaces. *Inter. Metals Rev.* 22: 262–301.
35. Zanaga D, Altantzis T, Sanctorum J, Freitag B, and Bals S (2016) An alternative approach for ζ-factor measurement using pure element nanoparticles. *Ultramicroscopy* 164: 11–16.
36. Fladischer S and Grogger W (2014) Quantitative EDXS analysis of organic materials using the ζ-factor method. *Ultramicroscopy* 136: 26–30.
37. Dolby R M (1963) An X-ray microanalyzer for elements of low atomic number. In: Pattee H H, Cosslett V E, and Engström A (eds), *Proceeding 3rd International Congress X-ray Optics and Microanalysis*, pp 483–493 (Academic Press, New York, NY).
38. Wikipedia: Ray Dolby https://en.wikipedia.org/wiki/Ray_Dolby.
39. Marvel C J, Behler K D, LaSalvia J C, Domnich V, Haber R A, Watanabe M, and Harmer M P (2019) Extending ζ-factor microanalysis to boron-rich ceramics: quantification of bulk stoichiometry and grain boundary composition. *Ultramicroscopy* 202: 163–172.
40. Rasberry S D (1987) *Certificate of Analysis for Standard Reference Material 2063*. (National Bureau of Standards now National Institute of Standards and Technology, Gaithersburg, MD).
41. Reed W P (1993) *Certificate of Analysis for Standard Reference Material 2063a*. (National Institute of Standards and Technology, Gaithersburg, MD).
42. Watanabe M and Wade C A (2013) Practical measurement of X-ray detection performance of a large solid-angle silicon drift detector in an aberration- corrected STEM. *Microsc. Microanal.* 19: 1264–1265.
43. Lyman C E, Goldstein J I, Williams D B, Ackland D W, von Harrach H S, Nicholls A W, and Statham P J (1994) High performance X-ray detection in a new analytical electron microscopy. *J. Microsc.* 176: 85–98.
44. Cosslett V E and Duncumb P (1956) Micro-analysis by a flying-spot X-ray method. *Nature* 177: 1172–1173.
45. Watanabe M (2013) Microscopy hacks: development of various techniques to assist quantitative nanoanalysis and advanced electron microscopy. *Microscopy* 62: 217–241.
46. Kothleitner G, Neish M J, Lugg N R, Findlay S D, Grogger W, Hofer F, and Allen L J (2014) Quantitative elemental mapping at atomic resolution using X-ray spectroscopy. *Phys. Rev. Lett.* 112: 085501.
47. Bullock J F, Humphreys C J, Mace A J W, Bishop H E, and Titchmarsh J M (1985) Crystalline effects in the analysis of semiconductor materials using Auger electrons or X-rays. *Microsc. Semicond. Mater.* 1985: 405–410.
48. Forbes B D, D'lfonso A J, Williams R E A, Srinivasan R, Fraser H L, McComb D W, Freitag B, Klenov D O, and Allen L J (2012) Contribution of thermally scattered electrons to atomic resolution elemental maps. *Phys. Rev. B* 86: 024108.
49. Kotula P G, Klenov D O, and von Harrach H S (2012) Challenges to quantitative multivariate statistic analysis of atomic-resolution X-ray spectral. *Microsc. Microanal.* 18: 691–698.
50. Lu P, Xiong J, van Benthem M, and Jia Q (2013) Atomic-scale chemical quantification of oxide interfaces using energy-dispersive X-ray spectroscopy. *Appl. Phys. Lett.* 102: 173111.
51. Chen Z, D'Alfonso A J, Weyland M, Taplin D J, Allen L J, and Findlay S D (2015) Energy dispersive X-ray analysis on an absolute scale in scanning transmission electron microscopy. *Ultramicroscopy* 157: 21–26.
52. MacArthur K E, Yankovich A B, Béché A, Luysberg M, Brown H G, Findlay S D, Heggen M, and Allen L J (2021) Optimizing experimental conditions for accurate quantitative energy-dispersive X-ray analysis of interfaces at the atomic scale. *Microsc. Microanal.* 27: 528–542.
53. Ishizuka K (2012) Prospects of atomic resolution imaging with an aberration– corrected STEM. *J. Electron Microsc.* 50: 291–305.
54. Watanabe M (2011) Chapter 7. X-ray energy dispersive spectrometry in scanning transmission electron microscopes. In: Pennycook S J and Nellist P D (eds), *Scanning Transmission Electron*

Microscopy: Imaging and Analysis, pp 291–351 (Springer, New York).

55. Fertig J and Rose H (1979) ON the theory of image formation in the electron microscope. II: signal-to-noise considerations on specimen resolution and quality of phase contrast images obtained by hollow cone illumination. *Optik* 54: 165–191.
56. Rose H (1981) Correction of aperture aberrations in magnetic systems with threefold symmetry. *Nuclear Inst. Methods* 187: 187–199.
57. Haider M, Uhlemann S, and Zach J (2000) Upper limits for the residual aberrations of a high-resolution aberration-corrected STEM. *Ultramicroscopy* 81: 163–175.
58. Doig P, Lonsdale D, and Flewitt P E J (1980) The spatial resolution of X-ray microanalysis in the scanning transmission electron microscope. *Philos. Mag. A* 41: 761–775.
59. Fiori C E, Swyt C R, and Myklebust R L (1992) *NIST/NIH Desk Top Spectrum Analyzer*, public domain software available from the National Institute of Standards and Technology Gaithersburg, MD through https://cstl.nist.gov/div837/Division/outputs/DTSA/oldDTSA.htm.
60. Wade C A, McLean M J, Vinci R P, and Watanabe M (2016) Aberration-corrected Scanning Transmission Electron Microscope (STEM) through-focus imaging for three-dimensional atomic analysis of bismuth segregation on copper [001]/33° twist bicrystal grain boundaries. *Microsc. Miroanal.* 22: 679–689.
61. Suenaga K, Tence M, Mory C, Colliex C, Kato H, Okazaki T, Shinohara H, Hirahara K, Bandow S, and Iijima S (2000) Element-selective single atom imaging. *Science* 290: 2280–2282.
62. Varela M, Findlay S D, Lupini A R, Christen H M, Borisevich A Y, Dellby N, Krivanek O L, Nellist P D, Oxley M P, Allen L J, and Pennycook S J (2004) Spectroscopic imaging of single atoms within a bulk solid. *Phys. Rev. Lett.* 92: 95502.
63. Suenaga K, Sato Y, Liu Z, Kataura H, Okazaki T, Kimoto K, Sawada H, Sasaki T, Omoto K, Tomita T, Kaneyama T, and Kondo Y (2009) Visualizing and identifying single atoms using electron energy-loss spectroscopy with low accelerating voltage. *Nature Chem.* 1: 415–418.
64. Senga R and Suenaga K (2015) Single-atom electron energy loss spectroscopy of light elements. *Nature Commun.* 6: 7943.
65. Lovejoy T C, Ramasse Q M, Falke M, Kaeppel A, Terborg R, Zan R, Dellby N, and Krivanek O L (2012) Single atom identification by energy dispersive X-ray spectroscopy. *Appl. Phys. Lett.* 100: 154101.
66. Stroud R, Lovejoy T, Falke M, Bassim N, Corbin G, Dellby N, Hrnčiřík P, Kaeppel A, Rohde M, and Krivanek O L (2015) Name that atom in 60 seconds or less: energy dispersive X-ray spectroscopy of individual heteroatoms in low dimensional materials. *Microsc. Microanal.* 21: 1427–1428.
67. Egerton R F, McLeod R, Wang F, and Malac M (2010) Basic questions related to electron-induced sputtering in the TEM. *Ultramicroscopy* 110: 991–997.
68. Rose A (1948) Television pickup tubes and the problem of vision. *Adv. Electron.* 1: 131–166.
69. Rose A (1970) Quantum limitations: to vision at low light levels. *Image Technol.* 12: 30–31.
70. Egerton R F and Watanabe M (2018) Characterization of single-atom catalysts by EELS and EDX spectroscopy. *Ultramicroscopy* 193: 111–117.
71. Egerton R F (2013) Document details - beam-induced motion of adatoms in the transmission electron microscope. *Microsc. Microanal.* 19: 479–486.
72. Suenaga K, Okazaki T, Okunishi E, and Matsumura S (2012) Detection of photons emitted from single erbium atoms in energy-dispersive X-ray spectroscopy. *Nat. Photonics* 6: 545–548.
73. Williams D B, Papworth A J, and Watanabe M (2002) High resolution X-ray mapping in the STEM. *J. Electron Microsc.* 51S: S113–S126.
74. Lyman C E (1987) Prospects for analytical electron microscopy by X-ray emission spectroscopy. In: Kirschner J, Murata K, and Venables J A (eds), *Physical Aspects of Microscopic Characterization of Materials*, pp 123–134 (AMF, O'Hare, IL). Scanning Microscopy International, Suppl.1
75. Newbury D E, Wollman D A, Irwin K D, Hilton G C, and Martinis J M (1999) Lowering the limit of detection in high spatial resolution microanalysis with the microcalorimeter energy dispersive X-ray spectrometer. *Ultramicroscopy* 78: 73–88.